nature communications

Article

https://doi.org/10.1038/s41467-024-55369-6

# On-site biosignal amplification using a single high-spin conjugated polymer

Received: 2 October 2024

Accepted: 5 December 2024

Published online: 04 January 2025

Check for updates

Gao-Yang Ge[1,4], Jingcao Xu[1,4], Xinyue Wang[2], Wenxi Sun[1], Mo Yang[2], Zi Mei[3], Xin-Yu Deng[1], Peiyun Li[1], Xiran Pan[1], Jia-Tong Li[1], Xue-Qing Wang[1], Zhi Zhang[1], Shixian Lv[1], Xiaochuan Dai[2] & Ting Lei[1]

On-site or in-sensor biosignal transduction and amplification can offer several benefits such as improved signal quality, reduced redundant data transmission, and enhanced system integration. Ambipolar organic electrochemical transistors (OECTs) are promising for this purpose due to their high transconductance, low operating voltage, biocompatibility, and suitability for miniaturized amplifier design. However, limitations in material performance and stability have hindered their application in biosignal amplification. Here, we propose using high-spin, hydrophilic conjugated polymers and a computational screening approach to address this challenge. We designed a high-spin polymer, namely P(TII-2FT), which exhibits satisfactory, stable, and balanced ambipolar OECT performance. The figure-of-merits achieved by the P(TII-2FT) devices surpass those of the current leading materials by 5 to 20 times, resulting in remarkable voltage gains while maintaining a compact form factor. Based on this amplifier, we have successfully achieved on-site capture and amplification of various electrophysiological signals with greatly enhanced signal quality.

Biosignal recording systems typically involve front-end signal transducers and downstream backend signal amplification, filtering, or feature detection components[1]. To mitigate noise, enhance signal quality, reduce redundant data transmission, and improve system integration, on-site or in-sensor signal processing has emerged as an increasingly significant avenue in bioelectronics[2,3]. Coating conducting polymers on electrodes can reduce interfacial impedance and improve the signal-to-noise ratio (SNR)[4,5]. Nevertheless, this approach lacks on-site amplification, and the large physical distance between the sensors and the backend signal processors introduces additional noise, resulting in compromised signal quality[6,7]. To achieve on-site amplification with compact form factors and exceptional performance, organic electrochemical transistors (OECTs), a burgeoning polymer-based bioelectronic technology[8–10], have garnered growing attention due to their low operating voltage (<0.8 V), remarkable flexibility/stretchability, high transconductance ($g_m$), and ability to form intimate biointerface[11].

OECTs have found utility in diverse biological applications, including metabolite sensing and electrophysiological recordings, with performance surpassing those of electrode-based sensors and inorganic transistors[12,13]. However, their current output presents challenges for practical implementation, given that most electrophysiology equipment demands a voltage input[14]. To tackle this issue, OECT-based circuits, such as unipolar circuits[15], complementary metal-oxide-semiconductor (CMOS)-like circuits[16] and ambipolar OECT-based circuits[14], have been devised (Supplementary Fig. 1). Ambipolar OECT-based circuits can enhance device integration, reduce footprint, and simplify manufacturing processes[14]. Nonetheless, the performance and stability of ambipolar OECT materials remain inadequate to meet the requirements of practical signal amplification. Moreover, achieving in vivo and on-site amplification within living organisms has yet to be realized, likely due to limitations in device stability and performance.

[1]National Key Laboratory of Advanced Micro and Nano Manufacture Technology, School of Materials Science and Engineering, Peking University, Beijing, China. [2]School of Biomedical Engineering, Tsinghua University, Beijing, China. [3]School and Hospital of Stomatology, Peking University, Beijing, China. [4]These authors contributed equally: Gao-Yang Ge, Jingcao Xu. e-mail: tinglei@pku.edu.cn

The past few years have witnessed rapid advancements in OECT materials, with p-type materials showcasing high $\mu C^*$ values exceeding 500 F cm$^{-1}$ V$^{-1}$ s$^{-1}$ and n-type materials demonstrating elevated $\mu C^*$ values surpassing 50 F cm$^{-1}$ V$^{-1}$ s$^{-1}$ [17–20]. In contrast, the current best ambipolar material is based on blending p-type and n-type materials, resulting in moderate yet unbalanced performance, with a p-type $\mu C^*$ of 22.8 F cm$^{-1}$ V$^{-1}$ s$^{-1}$ and an n-type $\mu C^*$ of 11.8 F cm$^{-1}$ V$^{-1}$ s$^{-1}$ [21]. Although this approach is straightforward, it offers limited performance and may lead to inadequate uniformity in large-area fabrication due to challenges in controlling the morphology and phase separation of the two OECT materials. Single-component ambipolar materials are more appealing, as they simplify device fabrication processes while promoting better film uniformity. However, their performance and stability remain subpar[14,22]. The most promising single-component ambipolar material, 2DPP-OD-TEG, exhibits a p-type $\mu C^*$ of 31.8 F cm$^{-1}$ V$^{-1}$ s$^{-1}$ and an n-type $\mu C^*$ of 6.8 F cm$^{-1}$ V$^{-1}$ s$^{-1}$, and its device performance drops rapidly after 84 cycles during p-type operation[22]. Thus, ambipolar OECT materials are underexplored, significantly trailing behind their p-type and n-type counterparts. In traditional OFET material design, achieving high-performance, stable, and balanced ambipolar characteristics is feasible through the use of classical low-bandgap donor-acceptor (D-A) polymers[23–25]. Nevertheless, our attempts indicate that this approach is not applicable to ambipolar OECT materials, primarily due to the challenge of restricted polaron delocalization and unstable doped states (see Supplementary Fig. 2 for detailed discussions)[18]. Consequently, the design strategy for achieving high-performance, stable, and balanced ambipolar OECT materials remains elusive.

Here, we propose designing high-spin conjugated polymers for high-performance, stable and balanced ambipolar OECTs. We have successfully developed a single-component ambipolar polymer, P(TII-2FT) (Fig. 1d), which demonstrates balanced and exceptionally high ambipolar properties with $\mu C^*$ values of 158.6 F cm$^{-1}$ V$^{-1}$ s$^{-1}$ for the p-type regime and 147.4 F cm$^{-1}$ V$^{-1}$ s$^{-1}$ for the n-type regime. These values are over 5 to 20 times higher than the current best single-component ambipolar materials. Our ambipolar OECTs also exhibited unprecedented stability with less than 6% current change after cycling over 1000 times. Computational studies corroborate that the design of high-spin polymers facilitates the effective delocalization and stabilization of positive and negative polarons, resulting in enhanced performance and much better stability. By leveraging this material, we have successfully realized NOT (Inverter), NAND, and NOR gates, as well as ultrahigh gain amplifiers. Furthermore, we harnessed the amplifiers to monitor human electrocardiograph (ECG), electroencephalograph (EEG), and mouse electrocorticogram (ECoG) signals. These biosignals experienced amplification exceeding 70 times, showcasing the immense potential of employing hydrophilic high-spin polymers for on-site biosignal capture and amplification.

## Results

### Polymer design, synthesis, and characterization

Compared with OFET materials, which work in neutral or lightly doped states, OECT materials generally operate in highly doped states[26], thus their charge delocalization capabilities and stability in the doped states are crucial[18]. We propose that a high-performance, stable, and balanced ambipolar OECT material requires (1) high charge carrier mobility, (2) stable p-doped and n-doped states and (3) balanced hole/electron injection/transport ability. To meet these requirements, we selected polymer building blocks through the following steps: (I) Most high-mobility conjugated polymers are based on several high-performance building blocks (e.g., bithiophene imide (BTI)[27], naphthalene diimide (NDI)[14,28], isoindigo (IID)[29], dithienyl diketopyrrolopyrrole (TDPP)[4], benzodifurandione-based oligo(*p*-phenylene vinylene) (BDOPV)[30], and thienoisoindigo (TII)[31]), primarily due to their good backbone planarity and strong interchain interactions. (II) The singlet-triplet energy gap ($\Delta E_{ST} = E_S - E_T$) represents the energy difference between the singlet and triplet states[32]. As the energy level of the singlet state approaches that of the triplet state, the organic

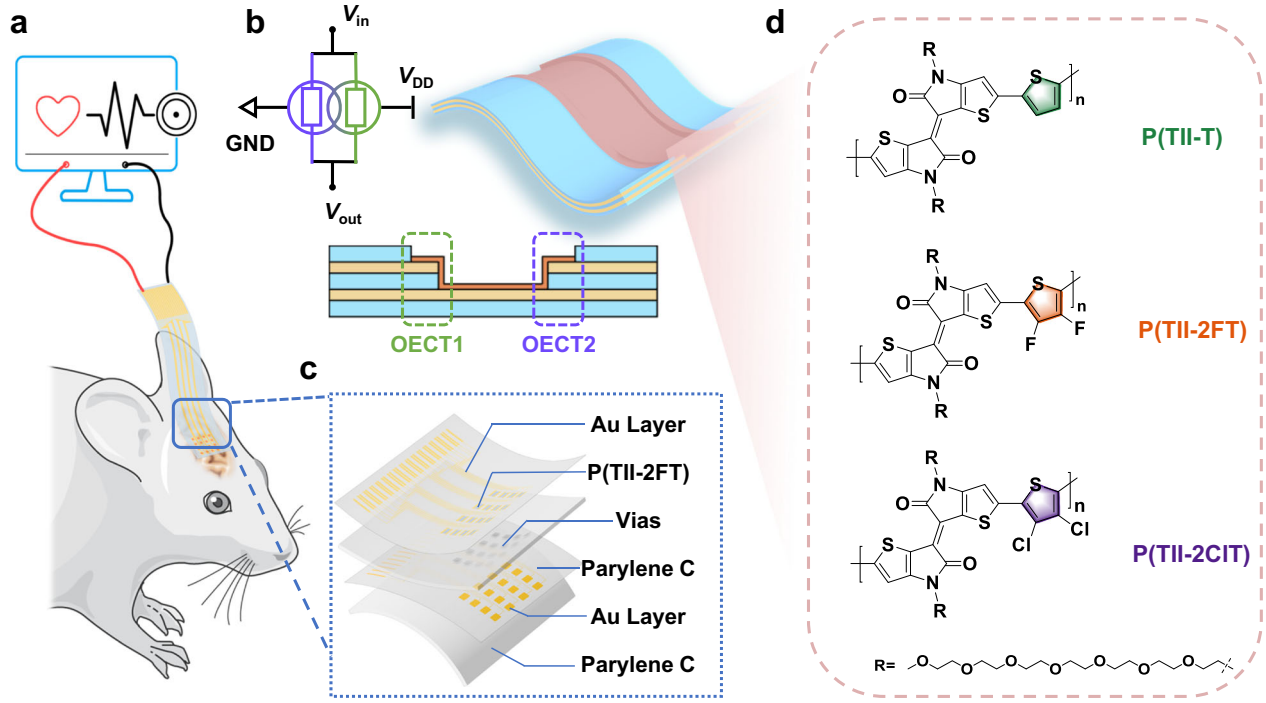


**Fig. 1 | Schematic illustration of using high-spin polymers for on-site biosignal amplification. a** Schematic illustration of a flexible OECT sensor matrix for capturing and amplifying mouse electrocorticogram (ECoG). **b** Diagram of the compact signal amplifier based on a cofacial vertical OECT pair and the corresponding circuit diagram. **c** The layered device configuration of our device. **d** Chemical structures of the three high-spin polymers, P(TII-T), P(TII-2FT), and P(TII-2ClT) used for this study. Panel **a** was partly generated using Servier Medical Art under a Creative Commons Attribution 3.0 unported license.

https://doi.org/10.1038/s41467-024-55369-6

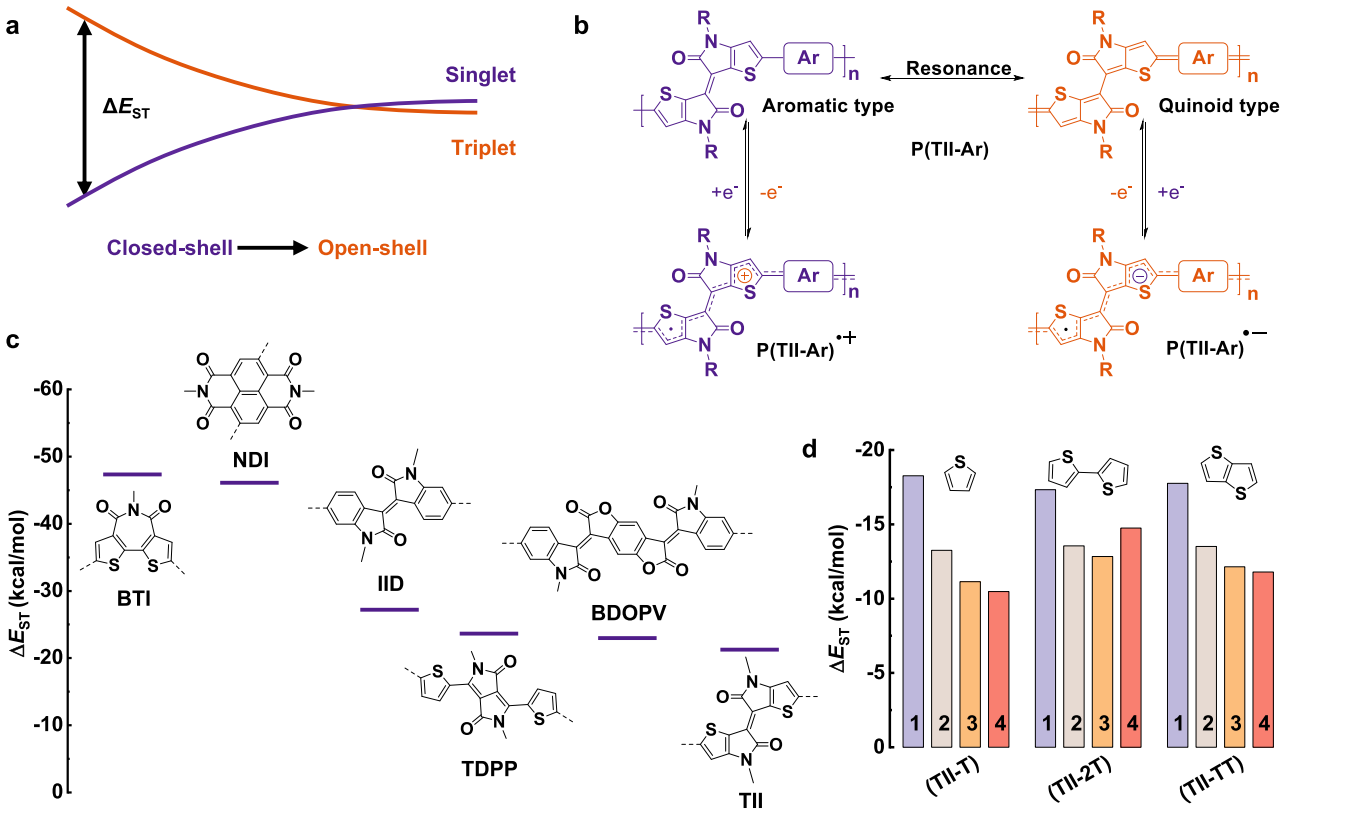


**Fig. 2 | Polymer design and characterization. a** Schematic illustration of the transition from a closed-shell state to an open-shell state as the energy gap between the singlet state and the triplet state decreases. **b** Resonance structures and the amphoteric redox behaviors of P(TII-Ar), which could encompass both aromatic type (closed-shell) and quinoid type (open-shell) structures. The "Ar" represents the comonomers. **c** Calculated $\Delta E_{ST}$ values of the six commonly used high-mobility building blocks. **d** Calculated $\Delta E_{ST}$ values of the three polymers: P(TII-T), P(TII-2T), and P(TII-TT). 1, 2, 3, and 4 represent the number of repeating units used for calculation.

semiconductor gradually transitions from a closed-shell to an open-shell character (Fig. 2a)[33]. Simultaneously, the degree of overlap between the highest occupied molecular orbital (HOMO) and the lowest unoccupied molecular orbital (LUMO) of the material increases, implying enhanced charge delocalization along the polymer backbone and further stabilizing the electronic structure in a high-spin state[34,35]. High-spin electronic structures usually exhibit rich redox behaviors[36,37], with two electrons occupying two nearly degenerate frontier orbitals, each capable of gaining or losing electrons. We propose that this characteristic could enable stable ambipolar charge transport after doping (Fig. 2b). (III) The polymers must also have a planar backbone for better intrachain/interchain charge transport.

Based on these assumptions, we screened available high-mobility building blocks by calculating their $\Delta E_{ST}$ values (Fig. 2c). Among them, TII exhibits the largest $\Delta E_{ST}$ value, suggesting that TII could possess the most significant open-shell character. Thiophene (T), bithiophene (2T), and thieno[3,2-b]thiophene (TT) are commonly used comonomers and were also employed for calculations. Compared to P(TII-2T) and P(TII-TT), P(TII-T) demonstrates the largest $\Delta E_{ST}$ value (Supplementary Table 1, Fig. 2d, and Supplementary Fig. 3). Thus, TII and T were selected for constructing the polymers. Based on P(TII-T), P(TII-2FT) and P(TII-2ClT) were also designed (Fig. 1d), with two fluorine or chlorine atoms introduced to tune the frontier orbital energy levels for balanced hole/electron injection. Ethylene glycol (EG) side chains were used to enhance the polymers' hydrophilicity. Detailed synthesis and characterization of the polymers can be found in Supplementary Fig. 4–7.

All the polymers display similar absorption features with optical bandgaps below 1 eV (Fig. 3a and Supplementary Table 2). Notably, the absorption spectrum of P(TII-T) shows a slight redshift compared to P(TII-2FT) and P(TII-2ClT) (Fig. 3a and Supplementary Fig. 8), largely due to its strong intramolecular charge transfer effects and strong interchain aggregation (Supplementary Figs. 9–11). The absorption spectrum of P(TII-2FT) reveals a pronounced vibronic absorption shoulder at ~1067 nm, suggesting that P(TII-2FT) has a more planar backbone in thin film, consistent with the relaxed potential energy surface calculations (Supplementary Fig. 12). To further quantify the backbone planarity, we used a planarization index $\langle\cos^2\varphi\rangle$[38], which ranges between 0 (perpendicular) and 1 (coplanar) (see Supplementary Information for more details). The calculated results show that $\langle\cos^2\varphi\rangle$ values for P(TII-T), P(TII-2FT), and P(TII-2ClT) are 0.69, 0.72, and 0.48, respectively. The higher $\langle\cos^2\varphi\rangle$ values indicate better backbone planarity for P(TII-T) and P(TII-2FT) relative to P(TII-2ClT). All the polymers display distinct reduction and oxidation peaks during electrochemical operation (Supplementary Fig. 13). The HOMO/LUMO energy levels were determined to be −4.59/−3.99 eV for P(TII-T), −4.76/−4.05 eV for P(TII-2FT), and −4.89/−4.03 eV for P(TII-2ClT), respectively, consistent with the density functional theory (DFT) calculations (Supplementary Table 2 and Supplementary Fig. 14). Spectroelectrochemistry was also performed. All the polymers showed new absorption peaks (>1250 nm) in the long-wavelength region with decreased neutral polymer absorption (800–1200 nm), irrespective of reduction or oxidation, which can be attributed to the formation of polarons/bipolarons after doping (Fig. 3b, c, Supplementary Fig. 15–17). These results suggest that the three polymers can be readily p-doped or n-doped, promising for ambipolar charge transport.

Electron paramagnetic resonance (EPR) spectroscopy is employed to assess the open-shell characteristics of the polymers. At room temperature, P(TII-2ClT), P(TII-2FT), and P(TII-T) all exhibited strong EPR signals (Fig. 3e). We also synthesized other polymers with

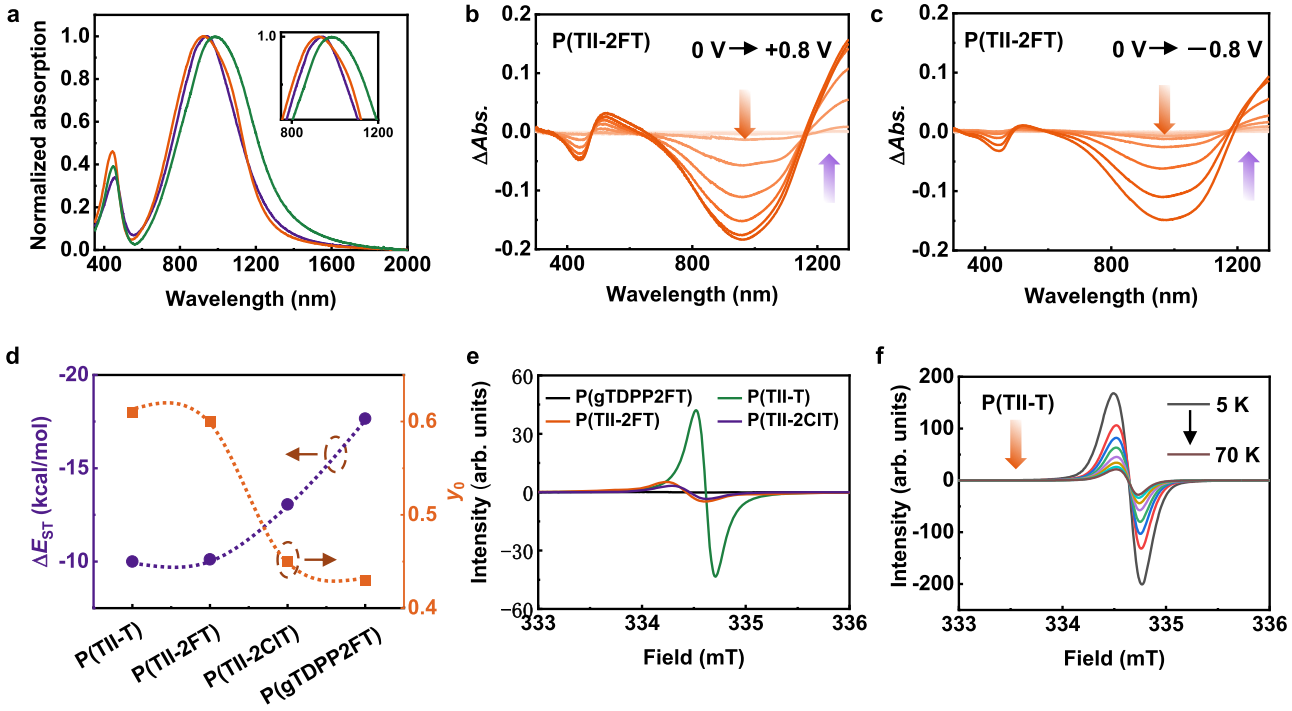


**Fig. 3 | Optoelectronic and electrochemical properties of the polymers.** **a** Normalized UV-vis-NIR absorption spectra of P(TII-T), P(TII-2FT), and P(TII-2ClT) in thin film. Electrochemical absorption spectra of P(TII-2FT) with **b** positive voltages (0 to +0.8 V) and **c** negative voltages (0 to −0.8 V) on ITO glass in 0.1 M NaCl aqueous solution. The Δ*Abs.* represents the difference in absorption intensity at various bias voltages. **d** Calculated $\Delta E_{ST}$ and $y_0$ values of the polymers. The $y_0$ value, ranging from 0 (closed-shell) to 1 (pure diradical), can be used to evaluate the diradical characteristic. **e** Comparison of the room-temperature EPR signals of the three polymers with P(gTDPP2FT) in the solid state. **f** Variable-temperature EPR signals of P(TII-T) in the solid state from 5 K to 70 K.

different building blocks (e.g., P(gTDPP2FT)) and side chains (e.g., alkyl chains) for comparison (Supplementary Figs. 12 and 18). All the results indicate the presence of unpaired electrons in their backbone and the polymers adopt an open-shell electronic structure. DFT-calculated $\Delta E_{ST}$ and $y_0$ values indicate that the order of the open-shell characteristics is as follows: P(TII-T) > P(TII-2FT) > P(TII-2ClT) (Fig. 3d and Supplementary Fig. 19). Compared to the closed-shell polymer P(gTDPP2FT) with a TDPP moiety, we can conclude that the open-shell characteristics of these polymers originate from the TII moiety. Variable-temperature EPR spectroscopy showed that both P(TII-T) and P(TII-2FT) exhibited a decreasing trend in EPR signals as the temperature increased (Fig. 3f and Supplementary Fig. 20), suggesting the presence of a triplet high-spin ground state in both materials[39,40].

## OECT device fabrication and characterization

The OECT devices based on the polymers were prepared using a photolithography and parylene patterning method[13]. The OECT performance of the polymers was characterized in an aqueous environment (0.1 M NaCl). All three polymers showed satisfactory ambipolar behaviors (Fig. 4a, b, and Supplementary Fig. 21–27). To evaluate the OECT performance of the polymers, the Bernards' model was used (Eq. 1)[41].

$$g_m = (W/L) \cdot d \cdot \mu \cdot C^* \cdot |(V_{Th} - V_{GS})| \quad (1)$$

where $g_m$, μ, and $C^*$ are the transconductance, charge carrier mobility, and volumetric capacitance; $W$, $L$, and $d$ are the channel width, length, and film thickness; $V_{Th}$ and $V_{GS}$ are the threshold voltage and the voltage between the gate and source electrodes. In the model, a figure-of-merit, $\mu C^*$, can be extracted to evaluate the performance of an OECT material[42]. The p-type/n-type $\mu C^*$ values are 122.2/16.4 F cm$^{-1}$ V$^{-1}$ for P(TII-T), 83.2/71.5 F cm$^{-1}$ V$^{-1}$ for P(TII-2FT), and 96.4/63.0 F cm$^{-1}$ V$^{-1}$ for P(TII-2ClT), respectively (Supplementary Table 3). It can be seen that the overall ambipolar steady-state performance of P(TII-2FT) is higher and more balanced. To achieve optimal OECT performance, the three polymers were further fractionated using preparative GPC to narrow the molecular weight distribution (Supplementary Fig. 28–35, and Supplementary Table 4). The purified P(TII-2FT) exhibited a remarkable p-type $\mu C^*$ of 158.6 F cm$^{-1}$ V$^{-1}$ and an n-type $\mu C^*$ of 147.4 F cm$^{-1}$ V$^{-1}$, setting a high standard for ambipolar OECT materials (Fig. 4f and Supplementary Table 5). Compared with P(TII-T) with a large n-type and small p-type $V_{Th}$ (0.76 V and −0.10 V), P(TII-2FT) and P(TII-2ClT) exhibited more balanced $V_{Th}$ values.

The $C^*$ values for OECTs operating in the p-regime/n-regime were measured to be 157/203 F cm$^{-3}$ for P(TII-T), 88/138 F cm$^{-3}$ for P(TII-2FT), and 180/214 F cm$^{-3}$ for P(TII-2ClT), respectively (Supplementary Fig. 36). These values are comparable to those of other high-performance OECT polymers[43,44]. Using $\mu C^*$ and $C^*$, the evaluated hole ($\mu_h$) and electron mobilities ($\mu_e$) of the polymers are 0.78/0.08 cm$^2$ V$^{-1}$ s$^{-1}$ for P(TII-T), 1.80/1.07 cm$^2$ V$^{-1}$ s$^{-1}$ for P(TII-2FT), and 0.54/0.30 cm$^2$ V$^{-1}$ s$^{-1}$ for P(TII-2ClT), respectively. These results indicate that P(TII-T) exhibits hole-dominant transport, whereas P(TII-2FT) and P(TII-2ClT) exhibit relatively balanced hole and electron transport. Compared with the pure n-type material P(gTDPP2FT)[18], P(TII-2FT) exhibits ideal ambipolar OECT characteristics by replacing the TDPP with TII. This highlights the efficacy of utilizing $\Delta E_{ST}$ to select the comonomer for ambipolar OECT materials. Furthermore, we evaluated the response speed of their OECT devices (Fig. 4c, d, Supplementary Figs. 37, and 38). All the polymers exhibited fast responses with $\tau_{on}/\tau_{off}$ on the scale of several milliseconds, comparable to the state-of-the-art p-type and n-type materials[44]. Under long-term cycling and continuous charging conditions, the stability of all three polymers significantly outperforms previously reported ambipolar polymers (Fig. 4g and Supplementary Figs. 39–41). For P(TII-2FT), it maintains 94% of the original current after 1000 cycles of cycling measurements in the air (Fig. 4e), and exhibits higher current retention under p-doped/n-doped operation (Supplementary Fig. 40). Furthermore, its OECT

https://doi.org/10.1038/s41467-024-55369-6

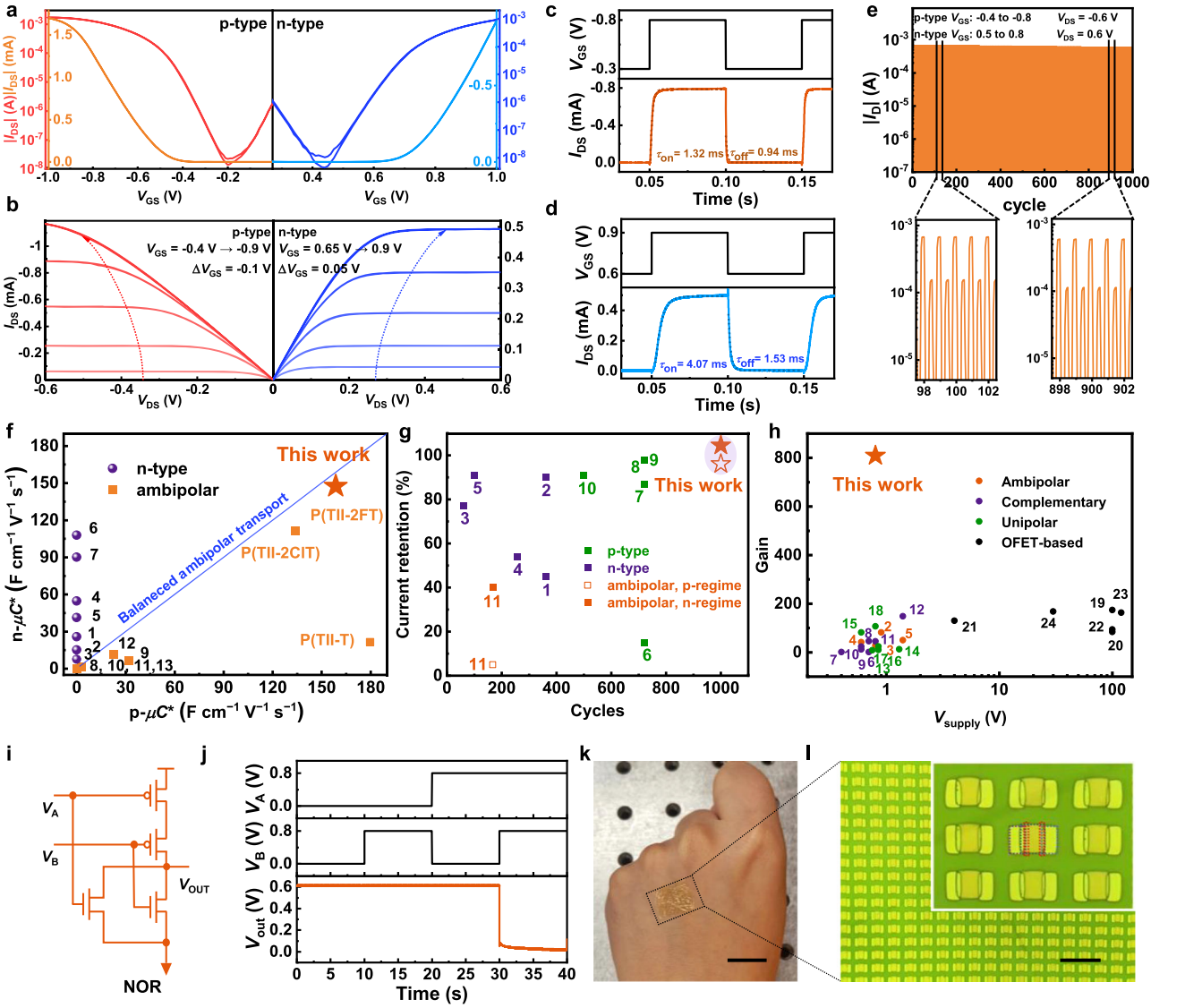


**Fig. 4 | OECT device and logic circuits fabrication and characterization.** **a** Transfer and **b** output characteristics based on P(TII-2FT) ($W/L$ = 100/10 μm). Transient response behavior of the **c** p-type and **d** n-type working regime of P(TII-2FT). **e** Operational stability over 1000 on-off cycling and alternating polarities of the OECT device. **f** Performance and **g** device stability comparison of our polymers with some state-of-the-art p-type, n-type, and ambipolar OECT materials (Supplementary Tables 5 and 6). **h** Comparison of the gain and supply voltage of the different types of inverters (Supplementary Table 7). **i** Circuit diagram and **j** voltage input and output behavior given by the NOR gate based on P(TII-2FT). **k** A flexible transistor array with 300 × 300 inverters attached to the back of a hand (scale bar: 1 cm). **l** Microscope image of the inverter array. Inset: enlarged microscope image of the inverter array (blue dashed line: $V_{DD}$ electrode contour; purple dashed line: $V_{SS}$ or $V_{GND}$ electrode contour; green dashed line: $V_{OUT}$ electrode contour; red dashed line: ambipolar OECT material channel contour; scale bar: 100 μm).

performance shows negligible changes after being stored in the air for 2 months (Supplementary Fig. 42), suggesting tremendous potential for large-scale integration in logic circuits and amplifiers. We also analyzed their polymer film microstructures and found that the higher crystallinity and minimal morphology change of P(TII-2FT) after doping might explain its excellent performance and satisfactory stability (Supplementary Figs. 43–46).

## Logic circuits fabrication and characterization

Recently, a new OECT device configuration, namely the cofacial vertical OECT (vOECT)[14], was proposed to increase the integration level and reduce the overall device size. However, this work only demonstrated moderate device performance due to poor OECT performance and stability. To fabricate high-performance single-component vOECT circuits, P(TII-2FT) has been employed to create vOECTs (Fig. 1b), in which two metal layers are separated by a parylene insulating layer serving as the source/drain contacts and interconnects. The thickness of the parylene layer roughly determines the vOECT channel length (0.5 μm), and the width of the OECT is defined by the etched area (100 μm) in photolithography (see Supplementary Information for more details). The vOECT inverters based on P(TII-2FT) demonstrated an ultra-high gain ($\partial V_{out}/\partial V_{in}$) of 809 V/V at a voltage step size of 0.1 mV with a simple device fabrication process (Supplementary Figs. 47 and 48). This gain, obtained under a low supply voltage ($V_{DD}$) of 0.8 V, is significantly higher than that of previously reported inverters based on OECTs and OFETs (Fig. 4h). Interestingly, we observed reduced inverter gains with larger voltage step sizes (Supplementary Fig. 49), showing a gain of 272 V/V at a 1 mV step and 30.1 V/V at a 10 mV step. NAND and NOR gates were also fabricated based on P(TII-2FT) (Fig. 4i, j, and Supplementary Fig. 50). We defined the output voltage below 0.05 V as '0' and the voltage above 0.55 V as '1'. All the devices showed correct logic operations, demonstrating the possible creation of complex logic circuits using a single material. Additionally, we successfully fabricated a flexible array consisting of 300 × 300

https://doi.org/10.1038/s41467-024-55369-6

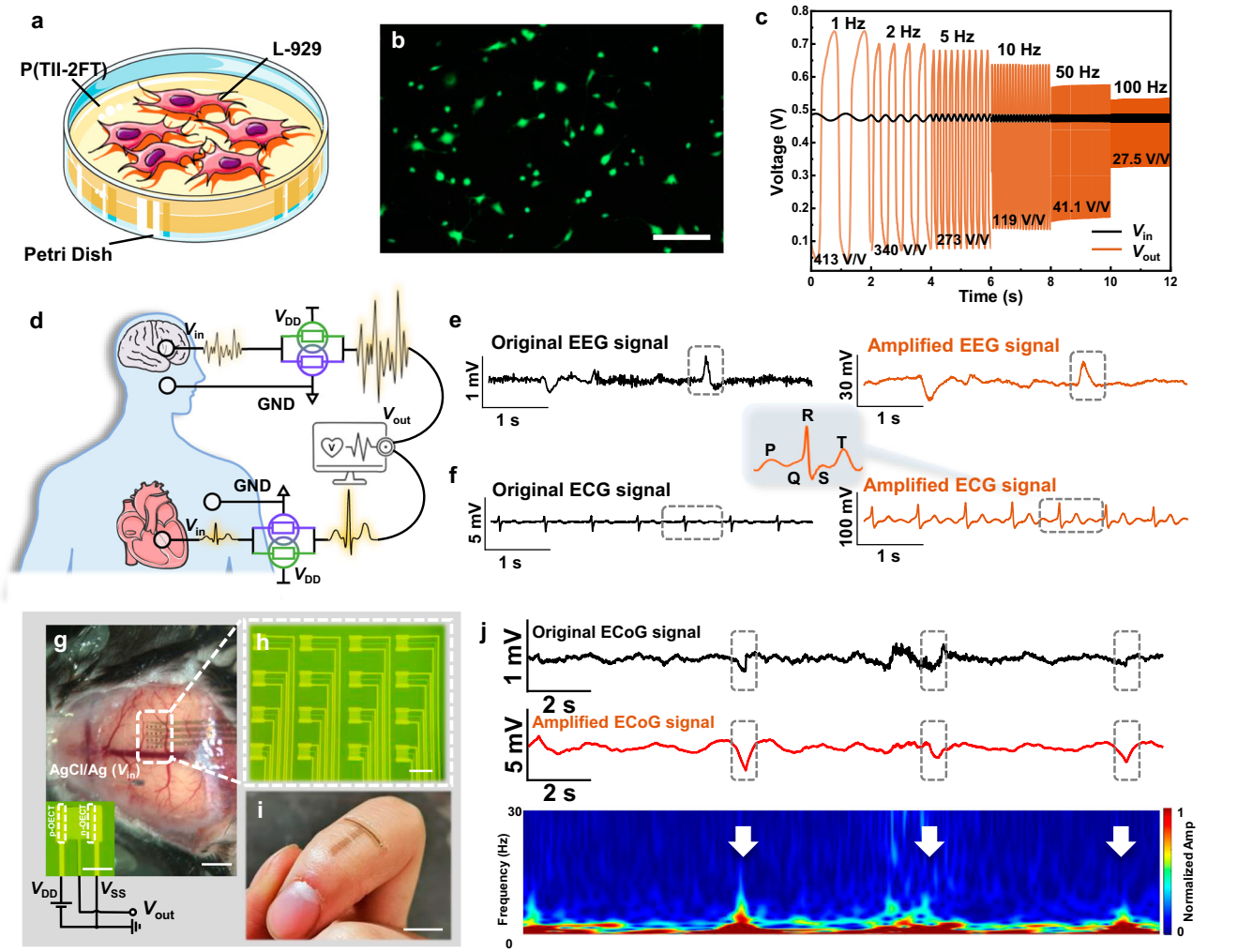


**Fig. 5 | Biosignal amplification using P(TII-2FT)-based amplifiers. a** Schematic illustration of cell viability tests on P(TII-2FT) film. **b** Live (green fluorescence)/dead (red fluorescence) staining of mouse fibroblasts (L929) on P(TII-2FT) film (scale bar: 100 μm). **c** Dynamic response of the amplifier using small sinusoidal signals at different frequencies. The corresponding gains at different frequencies are also displayed. **d** Schematic illustration of the vOECT amplifier for recording (**e**) EEG and **f** ECG signals. **g** Photograph of in vivo ECoG recording and schematic of the electrical wiring (scale bar: 2 mm, inset: 100 μm). **h** Microscopic image of the amplifier array (scale bar: 200 μm). **i** Photograph of an ultrathin (10 μm) and flexible amplifier array attached to a finger joint (scale bar: 1 cm). **j** The ECoG signals of the cortex in vivo recorded by a metal electrode or a P(TII-2FT) amplifier. The time-frequency analysis diagram of the signal from the amplifier. In the ECG, EEG, and ECoG signals, the black lines represent the electrode-collected signals, and the orange lines represent the signals from our amplifier. Panel **a** was partly generated using Servier Medical Art under a Creative Commons Attribution 3.0 unported license.

vOECT inverters, equivalent to an inverter density of 78,125 $cm^{-2}$ (Fig. 4k, l, and Supplementary Fig. 51), highlighting the significant advantage of the ambipolar vOECT device structure in enhancing device integration and reducing space occupation.

## On-site biological amplification

The biocompatibility of P(TII-2FT) was evaluated by cell viability tests. Live/dead staining results showed that all mouse fibroblasts (L929) cultured on the P(TII-2FT) film were alive (green fluorescence) with no significant difference compared to the control group, revealing low cytotoxicity and good biocompatibility of our polymers (Fig. 5a, b). The high gain of P(TII-2FT)-based inverters decreases significantly as the frequency increases (Fig. 5c), similar to other CMOS-like inverters (see below Supplementary Fig. 54 for more details). At a high frequency of 100 Hz, the gain still maintains a value of 27.5 V/V, demonstrating excellent voltage amplification capabilities and suitability for on-site sensing and amplification of electrophysiological signals. Subsequently, flexible amplifiers based on P(TII-2FT) were fabricated (see Supplementary Figs. 52 and 53 for more details) to capture and amplify human EEG (electroencephalogram), ECG (electrocardiogram), and mouse ECoG (electrocorticography) signals (Fig. 5). The EEG of participants before and during mental arithmetic tasks was utilized for testing[45]. We collected EEG signals synchronously using a conventional metal electrode and the amplifier. To eliminate power line interference, we applied a high-pass filter with a cutoff frequency of 3 Hz and a notch filter at 50 Hz (Fig. 5e). The amplifier exhibited an SNR of 21.5 dB, while the metal electrode only showed an SNR of 9.2 dB. Similarly, ECG signals can also be recorded by attaching an electrode to the subject's skin near the heart, enabling the capture of cardiac signals. The amplifier can amplify these signals with a high SNR of 31.9 dB, and the QRS complex peaks, P wave, and T wave are well duplicated (Fig. 5f), meeting the requirements of functional ECG recording. Remarkably, the output ECG signal achieved a magnitude of 46.3 mV, 73 times higher than the initial voltage collected by the conventional electrode (Fig. 5f). Such on-site amplifiers possess several advantages over conventional ECG detectors, including high gain, considerable SNR, compact size, and portability, which could facilitate remote ECG monitoring and cardiac disease diagnosis.

https://doi.org/10.1038/s41467-024-55369-6

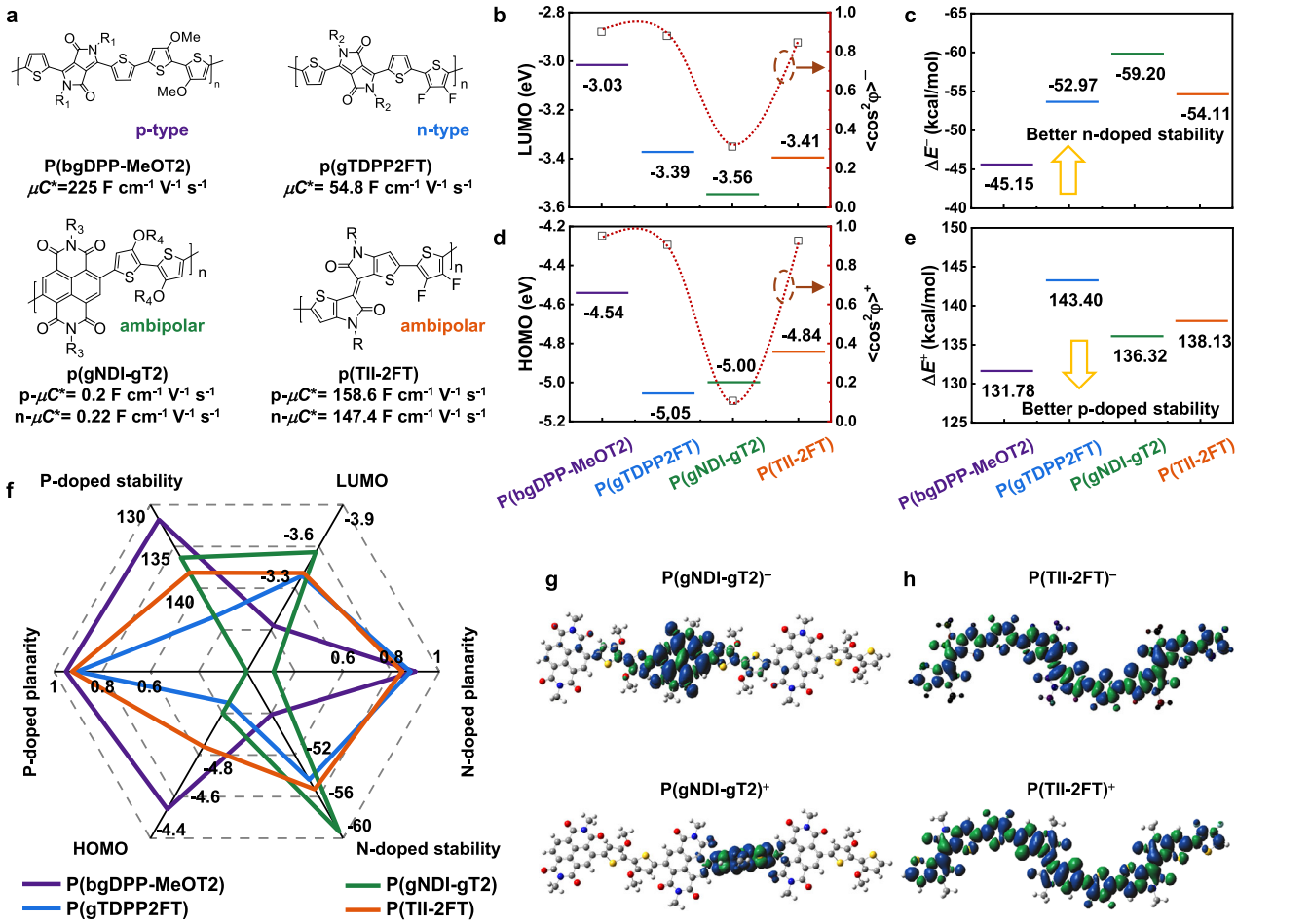


**Fig. 6 | Computational study and comparison of high-spin polymers and other OECT polymers. a** Chemical structures and $\mu C^*$ values of four polymers: P(bgDPP-MeOT2) (p-type); P(gTDPP2FT) (n-type); P(gNDI-gT2) (ambipolar), and P(TII-2FT) (ambipolar). The side chains of each polymer are omitted for clarity. **b** LUMO energy levels and n-doped backbone planarity. $\langle\cos^2\varphi\rangle^-$ is the $\langle\cos^2\varphi\rangle$ value of the polymer in an negatively charged state. **c** N-doped stability ($\Delta E^-$). **d** HOMO energy levels and p-doped backbone planarity. $\langle\cos^2\varphi\rangle^+$ is the $\langle\cos^2\varphi\rangle$ value of the polymer in a positively charged state. **e** P-doped stability ($\Delta E^+$). **f** Comparison of the six parameters affecting the device performance of the four polymers. Spin density distribution of the positively or negatively charged (**g**) P(gNDI-gT2) and **h** P(TII-2FT).

The voltage amplifiers were then used to record the electrocorticogram (ECoG) signals of the cortex in vivo. The voltage amplifiers were placed on the dura mater of a mouse after craniectomy. During the test, ECoG signals were collected using an AgCl/Ag electrode as the ground electrode and brain tissue fluid as the electrolyte (Fig. 5g). The devices successfully achieved on-site amplification (Fig. 5j), but compared to static tests and external electrode measurements, the amplification factor is only 5 to 10 times that of conventional electrodes. This unexpectedly low amplification factor might be due to the high signal frequency and complex solution environment within the brain tissue fluid (Supplementary Fig. 54). However, this does not mean that the quasi-static gain is insignificant for practical application. First, the quasi-static gain can be used to determine the suitable operating scenarios for an inverter. Smaller quasi-static measurement step aligns with smaller input signals, which could show larger gains. Quasi-static gain can also serve as an upper limit for actual amplification performance. Second, the gain may decrease at higher signal frequencies and is largely influenced by various environmental factors. Third, quasi-static gain also reflects the overall operational stability of an inverter (see Supplementary Fig. 54 for more details). Overall, we successfully realized on-site and in vivo biosignal capture and amplification using a single high-spin conjugated polymer, which provides a soft interface with tissues and could be further chemically modified for additional biofunctions, such as bioadhesion[11].

## Understanding of the high-spin conjugated polymer design

We propose six parameters (HOMO and LUMO energy levels, polaron stability, and backbone planarity after doping) to correlate our high-spin polymer design with ambipolar OECT performance (Fig. 6f). High-lying HOMO/low-lying LUMO energy levels can facilitate hole/electron injection from the source and drain electrodes[46]. $\Delta E^+$ and $\Delta E^-$ were proposed to evaluate polaron stability (or doped stability). $\Delta E^+$ represents the energy difference between the neutral and positively charged states ($\Delta E^+ = E_{positive} - E_{neutral}$), and a smaller $\Delta E^+$ value indicates better stability after p-doping, and vice versa. After doping, the backbone planarity may change[47], and a planar backbone can benefit charge transport. The $\langle\cos^2\varphi\rangle^{+/-}$ values were employed to evaluate polymer backbone planarity after p-doping/n-doping. All these parameters can be obtained using DFT calculations (see Supplementary Fig. 55 for more details).

Four representative polymers are used for comparisons (Fig. 6a–e)[18,48,49]. P(bgDPP-MeOT2) has a high-lying HOMO energy level and the highest stability and backbone planarity after p-doping, making it undoubtedly a p-type polymer. P(gTDPP2FT), featuring a low-lying LUMO energy level and better stability and backbone planarity after n-doping, is an n-type polymer. Both P(TII-2FT) and P(gNDI-gT2) span both p-type and n-type zones, exhibiting ambipolar behaviors. However, despite P(gNDI-gT2) having the lowest LUMO energy level and good stability in both p-doped and n-doped states, its ambipolar

OECT performance is much lower than that of P(TII-2FT). This is largely due to its twisted backbone after doping, leading to substantially lower charge carrier mobility (Fig. 6f). The spin density distribution of the charged P(gNDI-gT2) and P(TII-2FT) supports this observation (Supplementary Figs. 56–58). In the case of P(TII-2FT), the charges are uniformly distributed throughout the trimers, irrespective of being positively or negatively charged (Fig. 6h). For P(gNDI-gT2), the positive or negative charge is strongly localized (Fig. 6g), further impeding charge transport along the polymer backbone[50].

P(TII-2FT) shows balanced ambipolar behavior, while P(TII-T) is hole-dominated. This experimental result coincides with the six-parameter radar chart (Supplementary Fig. 61). P(TII-T) only satisfies the three parameters for the p-type regime, hence exhibiting high p-type and weak n-type OECT performance. In contrast, P(TII-2FT) matches the six parameters in both p-type and n-type regimes, displaying balanced p-type and n-type OECT performance. We further experimentally demonstrate that the unmatched LUMO energy level of P(TII-T) is the origin of its weak n-type performance (Supplementary Fig. 62). The obvious difference between the two high-spin polymers evidences that the high-spin electronic structure only endows the material with more stable polarons and good backbone planarity than traditional closed-shell polymers. However, the high-spin nature does not provide suitable HOMO/LUMO energy levels for efficient charge injection and balanced charge transport. Therefore, functional groups, such as fluorine or chlorine atoms, were introduced to tune the hole/electron injection. Both P(TII-2FT) and P(TII-2ClT) show more efficient electron injection than P(TII-T), indicating that suitable HOMO/LUMO energy level engineering is necessary for our high-spin polymer design. Supplementary Fig. 63 shows the relationships among our high-spin design, the six parameters, and ambipolar OECT performance. In addition to the TII polymer system, a widely used building block, TDPP, was employed to construct unique high-spin conjugated polymers. In this system, we employed high-spin monomers BT and TQ for design, and all the new polymers also show satisfactory ambipolar OECT performance (Supplementary Fig. 64–66), further demonstrating the generality and effectiveness of our high-spin polymer design strategy.

## Discussion

In summary, we have proposed a general and effective strategy to screen potential building blocks for designing high-performance, stable, and balanced ambipolar OECT polymers. The high-spin polymer, P(TII-2FT), demonstrates balanced and remarkable ambipolar properties, 5 to 20 times higher than current state-of-the-art materials, with satisfactory operational stability in aqueous media. Based on P(TII-2FT), we realized single-component flexible logic circuits and amplifiers with ultrahigh gains of over 800 V/V at a voltage step size of 0.1 mV. P(TII-2FT) also shows good biocompatibility, suitable for on-site biosignal amplification. Several biosignals, such as human ECG, EEG, and mouse ECoG, can be amplified using a single-component amplifier with a higher SNR than conventional electrodes. We believe this exceptional demonstration of single-component polymer in vivo amplifiers could enable more polymer-based bioelectronics with soft and multifunctional biointerfaces.

## Methods

The EEG and ECG measurements were approved by the Institutional Review Board (Approval number: PUIRB-2023139). These data were recorded from a male volunteer who is 24 years old at the time of the study (2024). And informed written consent was obtained prior to subject participation. The animal experiments were supervised and approved by the Animal Care & Use Committees at Tsinghua University (THU-LARC-2023-008). Our study is not related to the differences between individuals (e.g., age, gender, race, ethnicity, and racism). We only needed to ensure that the samples could provide valid biological signals.

### Materials

All the chemical reagents were purchased and used as received unless otherwise indicated. All air and water-sensitive reactions were performed under a nitrogen atmosphere. Dichloromethane (DCM), tetrahydrofuran (THF), toluene, and *N, N*-dimethylformamide (DMF) were dried using a JC Meyer solvent drying system before use. Ultradry solvents were obtained from J&K reagent company.

### Cytotoxicity

The sample substrate was preloaded into a 6-well plate. $5 \times 10^5$ mouse fibroblasts (L929) were seeded into each well and cultured in high glucose DMEM with 10% fetal bovine serum (FBS, 6021031, DAKEWE), 100 U/mL penicillin (Invitrogen), and 100 μ/mL streptomycin (Invitrogen) at 37 °C with 5% $CO_2$ and 95% humidity. After 24 h, a live/dead staining assay (cat# 40747ES76, Yeasen) was performed to evaluate the biocompatibility of the substrates. Briefly, cells were washed with 1×Assay Buffer. A working solution was prepared by adding 2 mM Calcein-AM solution and 1.5 mM PI solution to 5 mL of 1×Assay buffer. The working solution and assay buffer were added to the cell culture plates at a ratio of 1:2 and incubated at 37 °C for 15 min. Live cells (green fluorescence) and dead cells (red fluorescence) were excited with a 490 ± 10 nm laser (Nikon DS-F).

### Simulated EEG monitoring

The amplifier and the Au electrode, both with the same effective area on the same flexible device, were positioned on an agar model (2 wt%). An AgCl/Ag electrode was inserted into the model to simulate the EEG signal source. The signals from the Au electrode and amplifier were recorded using the Fs-Pro semiconductor parameter analyzer, PDA. MATLAB was used for software filtering. The signals were digitally filtered using a 50 Hz notch filter.

### Preparation for in vivo ECoG recording

For the in vivo experiments, mature female C57BL/6 mice, 8 weeks of age (Charles River Laboratories), were used throughout this study. The mice were maintained at 22 ± 1 °C with humidity ranging from 30% to 70% and were kept on a 12-h light/dark cycle, with ad libitum access to food. All 910 experiments were supervised and approved by the Animal Care & Use Committees at Tsinghua University (THU-LARC-2023-008). During the surgery, the mice were anesthetized with oxygen-vaporized isoflurane (3% for induction, 1.5–2% for maintenance, 0.5 L/min). Body temperature was maintained at 37 °C. Craniotomies (three craniotomies of 1 $mm^2$ for testing and larger craniotomy over 20 $mm^2$ for visualization) were performed on the skull to expose the cortical surface without removing the dura mater. One silver wire coated with silver chloride was inserted into the cortex to a depth of about 0.5 mm through the craniotomies, serving as the ground electrode. The flexible amplifier was placed in another opening. The craniotomy where the flexible amplifier was positioned was done in different locations revealing various cortical areas such as the motor (M1), somatosensory (S1), and primary visual (V1) cortices. During subsequent tests, a metal bar was affixed to the mouse's skull using dental methacrylate to stabilize the mouse's brain. The FPC connected to the flexible amplifier was secured to the metal fixed bar to prevent the device from moving on the mouse's brain.

### Reporting summary

Further information on research design is available in the Nature Portfolio Reporting Summary linked to this article.

## Data availability

The data that support the findings of this study are available from the corresponding authors upon request.

## Code availability

The code that supports the findings of this study is available from the corresponding authors upon request.

## References


1. Lin, Q. et al. Wearable multiple modality bio-signal recording and processing on chip: a review. *IEEE Sens. J.* **21**, 1108–1123 (2021).
2. Zhou, F. & Chai, Y. Near-sensor and in-sensor computing. *Nat. Electron.* **3**, 664–671 (2020).
3. Cea, C. et al. Enhancement-mode ion-based transistor as a comprehensive interface and real-time processing unit for in vivo electrophysiology. *Nat. Mater.* **19**, 679–686 (2020).
4. Musk, E. An integrated brain-machine interface platform with thousands of channels. *J. Med. Internet Res.* **21**, e16194 (2019).
5. Khodagholy, D. et al. Neurogrid: Recording action potentials from the surface of the brain. *Nat. Neurosci.* **18**, 310–315 (2015).
6. Tang, X., Shen, H., Zhao, S., Li, N. & Liu, J. Flexible brain–computer interfaces. *Nat. Electron.* **6**, 109–118 (2023).
7. Shen, K., Chen, O., Edmunds, J. L., Piech, D. K. & Maharbiz, M. M. Translational opportunities and challenges of invasive electrodes for neural interfaces. *Nat. Biomed. Eng.* **7**, 424–442 (2023).
8. Huang, W. et al. Vertical organic electrochemical transistors for complementary circuits. *Nature* **613**, 496–502 (2023).
9. Chen, J. et al. Highly stretchable organic electrochemical transistors with strain-resistant performance. *Nat. Mater.* **21**, 564–571 (2022).
10. Rivnay, J. et al. Organic electrochemical transistors. *Nat. Rev. Mater.* **3**, 17086 (2018).
11. Li, N. et al. Bioadhesive polymer semiconductors and transistors for intimate biointerfaces. *Science* **381**, 686–693 (2023).
12. Ohayon, D. et al. Biofuel powered glucose detection in bodily fluids with an n-type conjugated polymer. *Nat. Mater.* **19**, 456–463 (2020).
13. Khodagholy, D. et al. High transconductance organic electrochemical transistors. *Nat. Commun.* **4**, 2133 (2013).
14. Rashid, R. B. et al. Ambipolar inverters based on cofacial vertical organic electrochemical transistor pairs for biosignal amplification. *Sci. Adv.* **7**, eabh1055 (2021).
15. Cea, C. et al. Integrated internal ion-gated organic electrochemical transistors for stand-alone conformable bioelectronics. *Nat. Mater.* **22**, 1227–1235 (2023).
16. Romele, P. et al. Multiscale real time and high sensitivity ion detection with complementary organic electrochemical transistors amplifier. *Nat. Commun.* **11**, 3743 (2020).
17. Griggs, S. et al. The effect of residual palladium on the performance of organic electrochemical transistors. *Nat. Commun.* **13**, 7964 (2022).
18. Li, P., Shi, J., Lei, Y., Huang, Z. & Lei, T. Switching p-type to high-performance n-type organic electrochemical transistors via doped state engineering. *Nat. Commun.* **13**, 5970 (2022).
19. Wang, Y. et al. Acceptor functionalization via green chemistry enables high-performance n-type organic electrochemical transistors for biosensing, memory applications. *Adv. Funct. Mater.* https://doi.org/10.1002/adfm.202304103 (2023).
20. Yang, W. et al. High-performance n-type polymeric mixed ionic-electronic conductors: The impacts of halogen functionalization. *Adv. Mater.* https://doi.org/10.1002/adma.202305416 (2023).
21. Stein, E. et al. Ambipolar blend-based organic electrochemical transistors and inverters. *Nat. Commun.* **13**, 5548 (2022).
22. Samuel, J. J. et al. Single-component cmos-like logic using diketopyrrolopyrrole-based ambipolar organic electrochemical transistors. *Adv. Funct. Mater.* **31**, 2102903 (2021).
23. Yang, J. et al. Isoindigo-based polymers with small effective masses for high-mobility ambipolar field-effect transistors. *Adv. Mater.* **29**, 1702115 (2017).
24. Ni, Z. et al. Mesopolymer synthesis by ligand-modulated direct arylation polycondensation towards n-type and ambipolar conjugated systems. *Nat. Chem.* **11**, 271–277 (2019).
25. Li, Y.-F., Guo, Y.-L. & Liu, Y.-Q. Recent progress in donor-acceptor type conjugated polymers for organic field-effect transistors. *Chin. J. Polym. Sci.* **41**, 652–670 (2023).
26. Wang, S. et al. An organic electrochemical transistor for multimodal sensing, memory and processing. *Nat. Electron.* **6**, 281–291 (2023).
27. Feng, K. et al. Cyano-functionalized fused bithiophene imide dimer-based n-type polymers for high-performance organic thermoelectrics. *Adv. Mater.* **35**, 2210847 (2023).
28. He, T. et al. Site-specific chemical doping reveals electron atmospheres at the surfaces of organic semiconductor crystals. *Nat. Mater.* **20**, 1532–1538 (2021).
29. Zhou, Y.-Y. et al. Visualizing the multi-level assembly structures of conjugated molecular systems with chain-length dependent behavior. *Nat. Commun.* **14**, 3340 (2023).
30. Wang, Y. et al. Green synthesis of lactone-based conjugated polymers for n-type organic electrochemical transistors. *Adv. Funct. Mater.* **32**, 2111439 (2022).
31. Parr, Z. S. et al. From p- to n-type mixed conduction in isoindigo-based polymers through molecular design. *Adv. Mater.* **34**, 2107829 (2022).
32. Sun, Z., Ye, Q., Chi, C. & Wu, J. Low band gap polycyclic hydrocarbons: From closed-shell near infrared dyes and semiconductors to open-shell radicals. *Chem. Soc. Rev.* **41**, 7857–7889 (2012).
33. Stuyver, T. et al. Do diradicals behave like radicals? *Chem. Rev.* **119**, 11291–11351 (2019).
34. Hinz, A., Bresien, J., Breher, F. & Schulz, A. Heteroatom-based diradical(oid)s. *Chem. Rev.* **123**, 10468–10526 (2023).
35. Yuan, D., Liu, W. & Zhu, X. Design and applications of single-component radical conductors. *Chem* **7**, 333–357 (2021).
36. Mori, S. et al. Medium diradical character, small hole and electron reorganization energies and ambipolar transistors in difluoroenoheteroles. *Angew. Chem. Int. Ed.* **61**, e202206680 (2022).
37. Rudebusch, G. E. et al. A biradical balancing act: redox amphoterism in a diindenoanthracene derivative results from quinoidal acceptor and aromatic donor motifs. *J. Am. Chem. Soc.* **138**, 12648–12654 (2016).
38. Che, Y. & Perepichka, D. F. Quantifying planarity in the design of organic electronic materials. *Angew. Chem. Int. Ed.* **60**, 1364–1373 (2021).
39. Abe, M. Diradicals. *Chem. Rev.* **113**, 7011–7088 (2013).
40. Chen, X.-X. et al. High-mobility semiconducting polymers with different spin ground states. *Nat. Commun.* **13**, 2258 (2022).
41. Bernards, D. A. & Malliaras, G. G. Steady-state and transient behavior of organic electrochemical transistors. *Adv. Funct. Mater.* **17**, 3538–3544 (2007).
42. Inal, S., Malliaras, G. G. & Rivnay, J. Benchmarking organic mixed conductors for transistors. *Nat. Commun.* **8**, 1767 (2017).
43. Li, P. & Lei, T. Molecular design strategies for high-performance organic electrochemical transistors. *J. Polym. Sci.* **60**, 377–392 (2022).
44. Kukhta, N. A., Marks, A. & Luscombe, C. K. Molecular design strategies toward improvement of charge injection and ionic conduction in organic mixed ionic–electronic conductors for organic electrochemical transistors. *Chem. Rev.* **122**, 4325–4355 (2022).
45. Zyma, I. et al. Electroencephalograms during mental arithmetic task performance. *Data* **4**, 14 (2019).
46. Paterson, A. F. et al. On the role of contact resistance and electrode modification in organic electrochemical transistors. *Adv. Mater.* **31**, 1902291 (2019).

47. Xiao, M. et al. Charge transport physics of a unique class of rigid-rod conjugated polymers with fused-ring conjugated units linked by double carbon-carbon bonds. *Sci. Adv.* **7**, eabe5280 (2021).
48. Giovannitti, A. et al. N-type organic electrochemical transistors with stability in water. *Nat. Commun.* **7**, 13066 (2016).
49. Jia, H. et al. Engineering donor–acceptor conjugated polymers for high-performance and fast-response organic electrochemical transistors. *J. Mater. Chem. C* **9**, 4927–4934 (2021).
50. Fratini, S., Nikolka, M., Salleo, A., Schweicher, G. & Sirringhaus, H. Charge transport in high-mobility conjugated polymers and molecular semiconductors. *Nat. Mater.* **19**, 491–502 (2020).

## Acknowledgements

This work is supported by National Natural Science Foundation of China (T2425010 (Lei) and 22172085 (Dai)) and Beijing Natural Science Foundation (JQ22006 (Lei)). G.-Y. G. thanks the Boya Postdoctoral Fellowship of Peking University. The authors thank Prof. Shenzhen Xu for his insightful discussions on DFT calculations. We acknowledge Molecular Materials and Nanofabrication Laboratory (MMNL) and Materials Processing and Analysis Center, Peking University, for the use of instruments. The computational part is supported by the High-Performance Computing Platform of Peking University. The authors thank beamline BL14B1 (Shanghai Synchrotron Radiation Facility) for providing beam time.

## Author contributions

G.-Y.G. and J.X. contributed equally to this work. G.-Y.G., X.P., and X.-Q.W. synthesized the polymer and performed some characterization. J.X., P.L., and W.S. performed device fabrication and characterization. J.-T.L. performed AFM measurements. X.-Y.D. performed DFT calculations and EPR measurements. Z.M. and S.L. performed cell viability tests. X.W., M.Y., and X.D. performed mouse ECoG tests. G.-Y.G., J.X., Z.Z., and T.L. wrote the manuscript. All the authors revised and approved the manuscript.

## Competing interests

The authors declare no competing interests.

## Additional information

**Supplementary information** The online version contains supplementary material available at https://doi.org/10.1038/s41467-024-55369-6.

**Correspondence** and requests for materials should be addressed to Ting Lei.

**Peer review information** *Nature Communications* thanks the anonymous reviewers for their contribution to the peer review of this work. A peer review file is available.